Journal of Materials Chemistry A

Accepted Manuscript

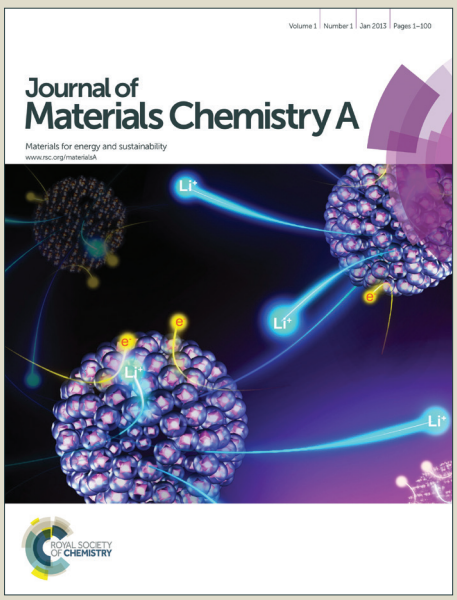

ROYAL SOCIETY OF CHEMISTRY

www.rsc.org/materialsA

Sodium deficient nickel-manganese oxides as intercalation electrodes in lithium ion batteries

M. Kalapsazova,[a] R. Stoyanova,[a*] E. Zhecheva [a], G. Tyuliev,[b] D. Nihtianova,[a,c]

The capability of sodium deficient nickel manganese oxides to participate in reactions of Li^+ intercalation and Na^+/Li^+ exchange allows to use them as low-cost electrode materials in lithium cells.

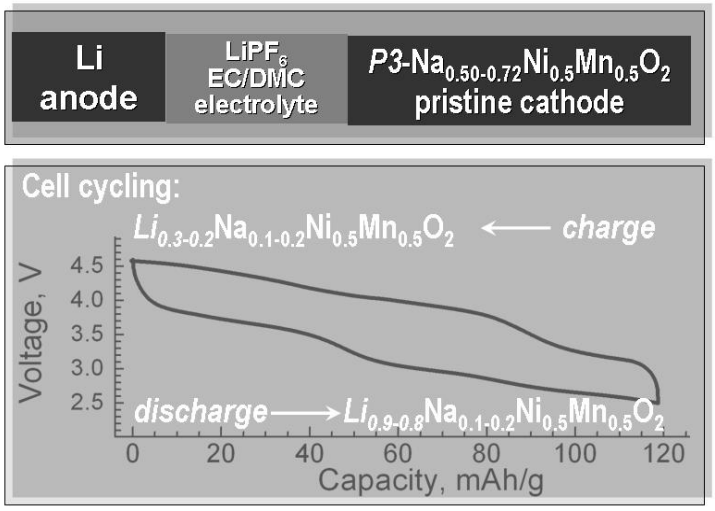

Cite this: DOI: 10.1039/c0xx00000x

ARTICLE TYPE

www.rsc.org/xxxxxx

Sodium deficient nickel-manganese oxides as intercalation electrodes in lithium ion batteries

M. Kalapsazova,[a] R. Stoyanova,[*a] E. Zhecheva,[a] G. Tyuliev [b] and D. Nihtianova [a,c]

Received (in XXX, XXX) Xth XXXXXXXXX 20XX, Accepted Xth XXXXXXXXX 20XX

DOI: 10.1039/b000000x

Sodium deficient nickel-manganese oxides $Na_xNi_{0.5}Mn_{0.5}O_2$ with a layered structure are of interest since they are able to participate in reactions of intercalation of Li^+ and exchange of Na^+ with Li^+. Taking into account the intercalation properties of these oxides, we provide new data on the direct use of $Na_xNi_{0.5}Mn_{0.5}O_2$ as low-cost electrode materials in lithium ion batteries instead of the lithium analogues. Sodium deficient nickel-manganese oxides $Na_xNi_{0.5}Mn_{0.5}O_2$ were prepared at 700 ^oC from freeze-dried acetate precursors. The structure of $Na_xNi_{0.5}Mn_{0.5}O_2$ is analyzed by means of powder X-ray diffraction, SAED and HRTEM. The oxidation states of nickel and manganese ions are determined by X-ray photoelectron spectroscopy (XPS) and electron paramagnetic resonance spectroscopy (EPR). Model lithium cells are used to monitor the lithium intercalation into $Na_xNi_{0.5}Mn_{0.5}O_2$. The surface and composition stability of $Na_xNi_{0.5}Mn_{0.5}O_2$ during the electrochemical reaction is followed by *ex-situ* XPS and LA-ICPMS. Layered oxides $Na_xNi_{0.5}Mn_{0.5}O_2$ exhibit a *P3*-type of structure, in which the solubility of sodium is limited between 0.5 and 0.75. At 700 ^oC, $Na_xNi_{0.5}Mn_{0.5}O_2$ consists of thin well-crystallized nanoparticles, some of the particles have sizes higher than 100 nm, displaying a trigonal superstructure. For all oxides, manganese ions occur in the oxidation state of +4, while the oxidation state of nickel ions is higher than +2 and depends on the sodium content. The electrochemical reaction is occurring within two potential ranges at 3.1 and 3.8 V due to the redox manganese and nickel couples, respectively. During the first discharge, Li^+ intercalation and Li^+/Na^+ exchange reactions are taking place, while the consecutive charge process include mainly Li^+ and Na^+ deintercalation. As a result, all oxides manifest reversible capacity of about 120 - 130 mAh/g, corresponding to 0.5-0.6 moles of Li^+. The formation of surface layers in the course of the electrochemical reaction is also discussed.

Introduction

Lithium transition metal oxides are the most commonly used electrode materials for lithium ion batteries.[1,2] This is a consequence of their specific structures and redox properties. The main representative is the lithium cobalt oxide, $LiCoO_2$.[1] The crystalline structure of $LiCoO_2$ is composed of layers of edge-shared CoO_6 octahedra, wherein Li^+ ions are sandwiched between the cobalt layers.[3] Based on the number of the CoO_2-layers in the unit cell and the sites occupied by Li, the structure of $LiCoO_2$ can be classified as *O3*-type.[4] (*O3*-type structure means that three layers are stacked in a sequence and octahedral occupancy for Li^+ is observed in the unit cell.) Because of the layered structure, $LiCoO_2$ is able to insert and remove lithium reversibly in high amount by intercalation reaction. Lithium intercalation takes place due to the reversible oxidation and reduction of Co ions at potential higher than 3.8 V (i.e. Co^{3+}/Co^{4+} ionic pairs).[1] Nowadays $LiCoO_2$ is one of the most successful electrode materials with application in commercial electronics.[1,2] However, $LiCoO_2$ is expensive and environmentally unfriendly. Therefore, new concepts are needed to reduce the cost and environmental impact of $LiCoO_2$.[1,2]

One approach to develop more suitable electrode materials is to replace toxic cobalt ions with more environmentally benign nickel and manganese ions.[5-7] Like $LiCoO_2$, mixed $LiNi_{0.5}Mn_{0.5}O_2$ oxide displays a layered structure classified as *O3*-type.[5,6] However, the electronic structure of both compositions is different. In $LiNi_{0.5}Mn_{0.5}O_2$, nickel and manganese ions occur in the oxidation state of (+2) and (+4), respectively.[8-10] As a result, $LiNi_{0.5}Mn_{0.5}O_2$ displays during reversible lithium intercalation a two-electron electrochemical reaction (i.e. redox couples Ni^{2+}/Ni^{4+}), a phenomenon that is generally considered to be rare for layered oxides.[7,9,11] The appearance of transition metal ions in different oxidation states determines some structural peculiarities of $LiNi_{0.5}Mn_{0.5}O_2$ in comparison to the ideally layered *O3*-type $LiCoO_2$. First, the close values of ionic radii of Li^+ and Ni^{2+} facilitate partial mixing of Li and Ni between the layers leading to the following cation distribution: $[Li_{1-\delta}Ni_\delta][Li_\delta Ni_{0.5-\delta}\ Mn_{0.5}]O_2$.[9,11,12] Second, Ni^{2+} and

Mn^{4+} are ordered in the transition metal layer in a way that creates two distinct sites forming a $\sqrt{3}\ a$ x $\sqrt{3}\ a$ x c unit cell.[13,14] The cationic distribution has an impact on the electrochemical performance of $LiNi_{0.5}Mn_{0.5}O_2$, such as the rate capabilities and cycling stability. Therefore, layered lithium–nickel–manganese oxides, $LiNi_{0.5}Mn_{0.5}O_2$, are considered to be the next generation of cathode materials, which are capable of displacing the widely used layered $LiCoO_2$ oxide.[3,4] Irrespective of the recent achievements in improving the electrochemical properties, lithium nickel manganese oxides still remain expensive electrode materials.

Searching for cheaper electrode materials, a new concept is recently proposed.[15-19] The concept aims at using directly sodium transition metal oxides as electrode materials instead of lithium analogues.[15-19] There are two reasons to choose sodium transition metal oxides. First of all, sodium is more abundant and it has a lower cost in comparison with Li. Second, sodium transition metal oxides display a layered structure like that of their lithium analogues. Because of the bigger ionic radius of Na^+ in comparison with that of Li^+, sodium transition metal oxides possess a larger interlayer space, which is beneficial both for a rapid exchange of Na^+ with Li^+ and for easier lithium diffusion. The direct use of sodium containing compounds as electrode materials in lithium ion batteries is beneficial especially in case of vanadium and manganese-based layered oxides such as $Na_xV_3O_8$,[16,17] $Na_{2/3}Mn_{1-x}Fe_xO_2$,[18] α-$Na_{0.66}MnO_{2.13}$.[15] Recently, we have demonstrated that sodium deficient nickel manganese oxides with a composition $Na_{0.67}Ni_{0.5}Mn_{0.5}O_2$ are also attractive as electrode materials in lithium ion batteries since they are able to intercalate lithium reversibly, as well as to exchange Na^+ for Li^+.[19] It is worth mentioning that the concept of direct use of sodium transition metal oxides differs from the conventional methodology for the synthesis of electrode materials by ionic exchange reactions prior to their operation in electrochemical cells. For example, $LiNi_{0.5}Mn_{0.5}O_2$ prepared by ion exchange of Na^+ with Li^+ in the framework of $NaNi_{0.5}Mn_{0.5}O_2$ is characterized with low amount of nickel ions in the LiO_2-layers and has an improved rate capability.[20]

In general, sodium nickel manganese oxides exhibit a more complex structure than the lithium analogues. This is a result of the ability of Na^+ to occupy either octahedral (*O*) or prismatic (*P*) crystallographic sites. Following the notation proposed by Delmas et al.,[4] the crystalline structure of sodium containing oxides can be classified either as *O3* or as *P3* and *P2*-types. There is a close structural relationship between *P3* and *O3*: by gliding of the $Ni_{0.5}Mn_{0.5}O_2$-layer, the *P3* structure is easily transformed into *O3*. On the contrary, the transformation of *P2* into *P3* requires scission of $Ni_{0.5}Mn_{0.5}$–O bonds. Depending on the Na-to-(Ni+Mn) ratio, sodium nickel manganese oxides can assume *O3*-, *P3*- and *P2*-types of structures.[21] When the Na-to-(Ni+Mn) ratio is equal to 1, stoichiometric sodium-nickel-manganese oxide $NaNi_{0.5}Mn_{0.5}O_2$ has an *O3*-type of structure.[22] The layered structure ensures the sodium mobility, as a result of which $NaNi_{0.5}Mn_{0.5}O_2$ can intercalate Na^+ reversibly. Based on the intercalation properties, Komaba et al.[22] have proposed stoichiometric $NaNi_{0.5}Mn_{0.5}O_2$ as a cathode material for sodium ion batteries, which can be regarded as a low-cost alternative of the lithium ion batteries. During electrochemical sodium deintercalation from $NaNi_{0.5}Mn_{0.5}O_2$ to $Ni_{0.5}Mn_{0.5}O_2$, it is established that a reversible structural transformation is occurring from the hexagonal *O3* into the hexagonal *P3"*-type structure via monoclinic *O'3,* hexagonal *P3*-types and monoclinic *P'3*.[22] In comparison with $NaNi_{0.5}Mn_{0.5}O_2$, the complete delithiation of $LiNi_{0.5}Mn_{0.5}O_2$ to $Ni_{0.5}Mn_{0.5}O_2$ leads to the transformation from the *O3*-type into the *O1*-type structure.[1]

Contrary to the stoichiometric $NaNi_{0.5}Mn_{0.5}O_2$, sodium deficient nickel manganese oxides assume *P2*- or *P3*-types of structures, the more stable modification is the *P2*-type arrangement.[23] Among several sodium-nickel-manganese oxides with nominal compositions $Na_xNi_{x/2}Mn_{1-x/2}O_2$ and $2/3 \leq x \leq 1$ [21], the well-known compound with *P2*-type structure is $Na_{2/3}Ni_{1/3}Mn_{2/3}O_2$ oxide with low nickel content.[23,24] The same composition displays also a *P3*-type structure only in the case when $Na_{2/3}Ni_{1/3}Mn_{2/3}O_2$ is obtained at low temperatures (i.e. around 700 °C) [23]. In the *P2*-type structure, Na has a higher diffusivity in comparison with the corresponding *O3*-type structure.[25] As a result, $Na_{2/3}Ni_{1/3}Mn_{2/3}O_2$ displays a good rate capability when it is used in sodium ion batteries.[25] After the increase of the sodium content from 2/3 to 1, a structure transition from *P2* into *O3* arrangement was found for $Na_xNi_{x/2}Mn_{1-x/2}O_2$ oxides.[21] Recently, we have prepared a sodium deficient analogue of *O3*-$NaNi_{0.5}Mn_{0.5}O_2$ by applying the acetate precursor method.[19] The oxide has a fixed $Na_{0.67}Ni_{0.5}Mn_{0.5}O_2$ composition and it forms a *P3*-type structure. The structural flexibility of sodium nickel manganese oxides to assume different layer stacking and symmetries is the main driving force to use them as electrode materials in both lithium and sodium ion batteries.

The aim of this communication is doubled: first, to determine the concentration range of the solubility of sodium in the *P3*-type of structure of $Na_xNi_{0.5}Mn_{0.5}O_2$, and second, to provide new insight into the reversible lithium intercalation in $Na_xNi_{0.5}Mn_{0.5}O_2$. For the preparation of $Na_xNi_{0.5}Mn_{0.5}O_2$, the acetate precursor method was chosen. The crystalline structure is analyzed by means of powder X-ray diffraction, SAED and HRTEM. The oxidation state of nickel and manganese ions is determined by X-ray photoelectron spectroscopy (XPS) and electron paramagnetic resonance spectroscopy (EPR). Model lithium cells are used to monitor the lithium intercalation into $Na_xNi_{0.5}Mn_{0.5}O_2$. Bulk and surface changes during the lithium intercalation are followed by *ex-situ* XPS and laser ablation inductively coupled plasma mass spectrometry (LA-ICPMS).

Experimental

Sodium-nickel-manganese oxides are prepared from freeze-dried acetate precursors. The procedure of the preparation is given elsewhere.[19] The homogeneous acetate precursors were prepared by freeze-drying of the corresponding Na, Ni and Mn acetate solutions (0.5 M). The nominal Na-to-(Mn+Ni) ratio was 0.50, 0.67, 0.75 and 1.0. The freeze-drying process was performed with an Alpha-Crist Freeze-Dryer at -20 °C in vacuum. The freeze-dried acetate precursors are decomposed at 400 °C in O_2 atmosphere for 3 hours. After thermal decomposition of the precursors, the solid residue was homogenized, pelleted and annealed at 700 °C in air for 24 hours, followed by cooling down to room temperature. For the sake of convenience, $Na_xNi_{0.5}Mn_{0.5}O_2$ with nominal x=0.50 and x=0.67 will be

denoted further by NM050 and NM067.

The X-ray structural analysis was made by a Bruker Advance 8 diffractometer with LynxEye detector using CuKα radiation. Step-scan recordings for structure refinement by the Rietveld method are carried out using 0.02° 2θ steps of 4 s duration. The diffractometer zero point, the Lorentzian/Gaussian fraction of the pseudo-Voigt peak function, the scale factor, the unit cell parameters, the thermal factors and the line half-width parameters were determined. The computer FullProf Suite Program (1.00) was used in the calculations.[26]

The local structure and morphology of $Na_xNi_{0.5}Mn_{0.5}O_2$ was observed by JEOL 2100 transmission electron microscope at accelerating voltage of 200 kV. The specimens are prepared by grinding and dispersing the powders in ethanol by ultrasonic treatment for 6 minutes. The suspensions are dripped on standard holey carbon/Cu grids.

XPS was carried out using ESCALAB MkII (VG Scientific) electron spectrometer at a base pressure in the analysis chamber of $5x10^{-10}$ mbar (during the measurement 1 x 10^{-8} mbar), using MgKα X-ray source (excitation energy hν=1253.6 eV) and AlKα X-ray source (excitation energy hν=1486.6 eV). The instrumental resolution measured as the full width at a half maximum (FWHM) of the $Ag3d_{5/2}$, photoelectron peak is about 1 eV. The energy scale is corrected with respect to the C1s - peak maximum at 285 eV for electrostatic charging. The fitting of the recorded XPS spectra was performed, using a symmetrical Gaussian-Lorentzian curve fitting after Shirley-type subtraction of the background.

The EPR spectra were recorded as the first derivative of the absorption signal of an ERS-220/Q spectrometer within the temperature range of 90-400 K. The *g* factors were determined with respect to a Mn^{2+}/ZnS standard. The signal intensity was established by double integration of the experimental EPR spectrum. To facilitate the analysis of the EPR spectra of sodium compounds, the EPR standards for layered lithium analogues $Li_xNi_{1/2}Mn_{1/2}O_2$ was used. The EPR standards were obtained by electrochemical extraction of Li from $LiNi_{1/2}Mn_{1/2}O_2$.

The electrochemical charge-discharge behaviour of the $Na_xNi_{0.5}Mn_{0.5}O_2$ was examined by using two-electrode cells of the type Li | $LiPF_6$ (EC:DMC) |$Na_xNi_{0.5}Mn_{0.5}O_2$. The positive electrode, supported onto an aluminium foil, represented a mixture, containing 80% of the active composition $Na_xNi_{0.5}Mn_{0.5}O_2$, 7.5% C-NERGY KS 6 L graphite (TIMCAL), 7.5% Super C65 (TIMCAL) and 5% polyvinylidene fluoride (PVDF). The electrolyte contains 1M $LiPF_6$ solution in ethylene carbonate and dimethyl carbonate (1:1 by volume) with less than 20 ppm of water. Lithium electrodes consisted of a clean lithium metal disk with diameter of 15 mm. The cells were mounted in a dry box under Ar atmosphere. The electrochemical reactions were carried out using an eight-channel Arbin BT2000 system in galvanostatic mode. The cell is cycled at C/100 and C/20 rates.

The compositions of electrodes after the electrochemical reaction were determined by LA-ICPMS. The equipment consists of PerkinElmer ELAN DRC-e ICP-MS and state of the art New Wave UP193FX laser ablation system. The laser beam can analyze spots from 10 microns to 150 μm.

Results and Discussions

Structure of sodium deficient nickel-manganese oxides

XRD patterns of oxides with a nominal Na-to-(Ni+Mn) ratio varying between 0.5 and 1.0 are given in Figure 1. All XRD patterns display diffraction peaks that can be assigned to a mixture of the main layered phase and the impurity NiO-like phase. Therefore, the XRD patterns are calculated based on the structural model that comprises two phases: (i) layered phase with Na in two *3a* sites (0, 0, z_{Na}) and (1/3, 2/3, z_{Na}), Ni/Mn in *3a* sites (0, 0, 0) and oxygen in *3a* sites (0, 0, z_{O1}) and (0, 0, z_{O2}) for a *R3m* space group, and (ii) NiO phase with Ni and O in (0.5, 0.5, 0.5) and (0, 0, 0) sites for a space group *Fm-3m*. The amount of NiO impurity is less than 1% and it is insensitive towards the nominal Na-to-(Ni+Mn) ratio. This means that the solubility of Ni into Na_xMnO_2 is limited up to 0.5, which is in agreement with previously reported data.[23,24] On the other hand, the synthesis of $Na_xNi_{0.5}Mn_{0.5}O_2$ resembles the formation of high-voltage $LiNi_{1/2}Mn_{3/2}O_4$ spinel, where the impurity NiO-like phase pursues always the target phase.[27]

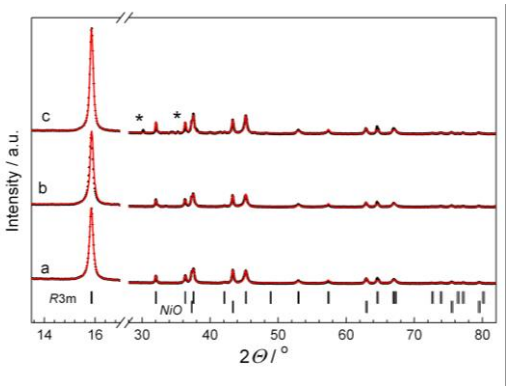

Figure 1 XRD patterns of $Na_xNi_{0.5}Mn_{0.5}O_2$ with nominal sodium contents of Na/(Ni+Mn)=0.5 (a); 0.67 (b) and 1.0 (c). The asterisk denotes Na_2CO_3 impurity.

According to the nomenclature, proposed by Delmas et al.,[4] sodium deficient nickel manganese oxides $Na_xNi_{0.5}Mn_{0.5}O_2$ can be denoted as *P3*-type structure. The lattice parameters of the main layered phase are given in Table 1. By increasing the nominal Na-(Ni+Mn) ratio from 0.5 to 1.0, the *a*-parameter shows a weak tendency to increase, which is opposite to the observed trend for the *c*-parameter. As a result, the lattice volume remains unchanged. In the layered phase, both Ni and Mn occupy the octahedral positions with a Ni,Mn-O bond length insensitive towards the variation in the nominal Na-(Ni+Mn) ratio, while sodium falls in a prismatic site with three long and three short Na-O bond lengths. It seems that the extent of prismatic deformation (expressed by the difference between the long and short Na-O bond length) is smaller for the oxide with nominal Na-(Ni+Mn)-ratio of 0.5 (Table 1).

To rationalize the slight dependence of the lattice parameters and the metal-oxygen bond lengths on the chemical composition, Table 1 represents the refined sodium occupancy in 3a sites. The refined sodium content increases with the nominal Na-to-(Ni+Mn) ratio reaching a maximal value of about 0.72 for Na-to-(Ni+Mn) ratio higher than 0.7. This means that the solubility of sodium in the layered *P3*-structure $Na_xNi_{0.5}Mn_{0.5}O_2$ is restricted between 0.5 and 0.72 mole. The excess of sodium remains as impurity phase in the form of sodium carbonates, which is hardly

Table 1 Structural parameters (a, c, V, z_{Na}, z_{O1}, z_{O2}), refined sodium content (Na_{XRD}) and mean Ni,Mn-O and Na-O bond lengths for $Na_xNi_{0.5}Mn_{0.5}O_2$ with a nominal sodium content of x=0.5, 0.67, 0.75 and 1.0. Intercalated Li amount and average oxidation state of transition metal ions (OS_{TMI}) determined based on the first discharge.

Nominal *x* in $Na_xNi_{0.5}Mn_{0.5}O_2$	*a* ± 0.0001, Å	*c* ± 0.0020, Å	V ± 0.02, Å^3	z_{Na}	z_{O1}/ z_{O2}	Na_{XRD} ± 0.003	MnNi-O, Å	Na-O, Å (3 long / 3 short lengths)	Li^+ amount	OS_{TMI}
0.50	2.8861	16.7908	121.13	0.8245	0.3868 / 0.6106	0.552	1.914	2.418 / 2.607	0.43	3.43
0.67	2.8867	16.7692	121.01	0.8229	0.3919 / 0.6100	0.682	1.918	2.337 / 2.618	0.31	3.31
0.75	2.8868	16.7748	121.06	0.8250	0.3911 / 0.6110	0.717	1.911	2.370 / 2.605	0.28	3.28
1.0	2.8871	16.7729	121.00	0.8260	0.3930 / 0.6116	0.724	1.911	2.371 / 2.603	0.29	3.29

visible on the XRD patterns of $Na_xNi_{0.5}Mn_{0.5}O_2$ with higher nominal sodium content (Fig. 1). The concentration limits for sodium solubility in the *P3*-type structure are comparable with those determined for $Na_xNi_{0.5}Mn_{0.5}O_2$, obtained during the electrochemical deintercalation of Na^+ out of stoichiometric $NaNi_{0.5}Mn_{0.5}O_2$ ($0.55<x<0.75$).[22]

Local structure of $Na_xNi_{0.5}Mn_{0.5}O_2$

Because of the low-temperature of synthesis, TEM analysis of $Na_xNi_{0.5}Mn_{0.5}O_2$ is undertaken as a next level of structure refinement. Figure 2 summarizes the bright field images and the electron diffractions for NM05 and NM067. Both NM05 and NM067 oxides consist of thin flat particles with dimensions covering a broad size range: from 20 to 160 nm (Figs. 2a). Polycrystalline diffractions support the formation of *P3*-type structure for $Na_xNi_{0.5}Mn_{0.5}O_2$ (Fig. 2a). All particles are well crystallized and well shaped (Fig. 2). For particles with sizes less than 60 nm, well resolved lattice fringes corresponding to the (003) plane (*d*-value of 0.56 nm) are observed (Fig. 2b). Bigger particles (sizes higher than 100 nm) display a hexagon-like shape. The SAED of some of them demonstrates the appearance of a trigonal superstructure with a=10.0 and c=33.5 Å and $P3_1$ space group (Fig. 2c). The superstructure can be represented as $\sqrt{12}\,a$ x $\sqrt{12}\,a$ x $2c$. The superstructure reflections are hardly visible for NM050 in comparison with NM067, therefore indicating a dependence of the supercell formation on the sodium content. Dahn *et al.* have also found a superstructure for both *P3*- and *P2*-$Na_{2/3}Ni_{1/3}Mn_{2/3}O_2$ modifications, where $\sqrt{3}\,a$ x $\sqrt{3}\,a$ superlattice is due to Ni/Mn ordering inside the transition metal layers.[23,24] In sodium deficient oxides studied by us, the large superlattice occurs in case of $Na_{2/3}Ni_{0.5}Mn_{0.5}O_2$: $\sqrt{12}\,a$ x $\sqrt{12}\,a$ x $2c$. This is not an unusual phenomenon if we take into account the strong tendency of sodium ions and vacancies to order inside the intralayer space.[28,29] For example, an exceptionally large superlattice (i.e. $\sqrt{12}\,a$ x $\sqrt{12}\,a$ x $3c$) has only been detected in case of sodium deficient cobaltates *P2*-Na_xCoO_2 with x=0.71 and has been explained as a result of the long-range three-dimensional sodium/vacancy ordering.[28,29] The superstructure of Na_xCoO_2 is extracted from the *P2*-type structure. There are two space groups proposed to fit the large superlattice: *R*-3c and $P3_1$.[28,29] The most appropriate space group for superlattice ordering of $Na_xNi_{0.5}Mn_{0.5}O_2$ appears to be $P3_1$. The common structural features of Na_xCoO_2 and $Na_xNi_{0.5}Mn_{0.5}O_2$ indicate that sodium/vacancy ordering is a main driving force for the formation of a large superlattice. This is an interesting phenomenon, which needs further studies to be elucidated.

Oxidation state of transition metal ions

Knowledge of the oxidation state of transition metal ions in $Na_xNi_{0.5}Mn_{0.5}O_2$ is critical for the interpretation of their electrochemical properties. To identify the oxidation state of Mn and Ni ions in sodium deficient oxides, X-ray photoelectron spectroscopy is applied. As a reference for Mn^{4+} and Ni^{2+}, we used the $LiNi_{0.5}Mn_{0.5}O_2$ analogue. Figure 3 compares the Mn 2p3/2 and Mn2p1/2 spectra of oxides with x=0.5 and x=0.67. The spectral parameters are summarized in Table 2. All spectra display two broad lines with maxima that coincide with the binding energies of the reference Mn^{4+}. However, the exact oxidation state of Mn ions is difficult to determine based on the Mn2p spectra only due to their complex multiplet structure. For Mn^{4+}, Mn^{3+} and Mn^{2+} free ions, Gupta and Sen calculated the multiplet structure and demonstrated that the Mn 2p3/2 spectrum of each single oxidation state consists of four or five multiplet emission lines separated from one another by 0.7–1.2 eV.[30]

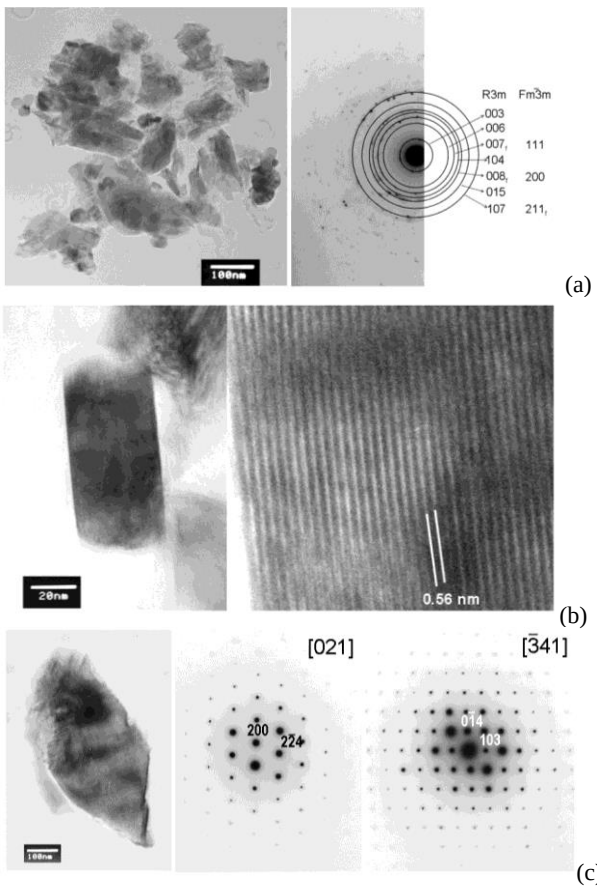

Figure 2 (a) Bright field micrograph and polycrystalline diffraction for $Na_{0.5}Ni_{0.5}Mn_{0.5}O_2$. (b) Bright field micrograph and corresponding HRTEM image for $Na_{0.67}Ni_{0.5}Mn_{0.5}O_2$. (c) Bright field micrograph and corresponding SAED for $Na_{0.67}Ni_{0.5}Mn_{0.5}O_2$, demonstrating the formation of trigonal superstructure ($P3_1$ space group).

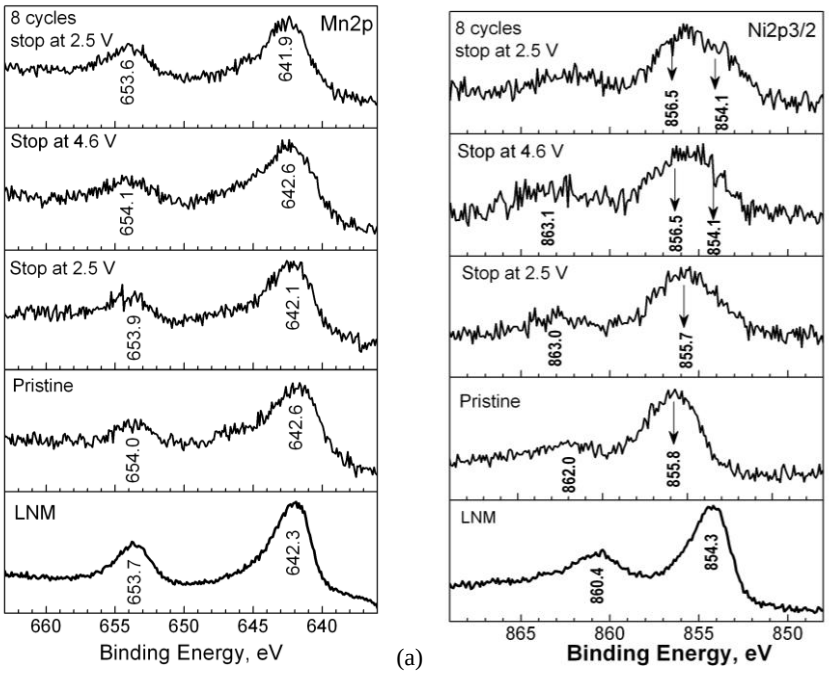

Figure 3 XPS spectra in the Mn2p (a) and Ni2p3/2 (b) regions for pristine NM067 and their counterparts used as electrodes in model lithium cells. For the sake of comparison, the XPS spectra for Ni^{2+} and Mn^{4+} references in $LiNi_{0.5}Mn_{0.5}O_2$ are also given

Another parameter that allows a more precise identification of the oxidation state of Mn is the 3s core binding energy.[31,32] For manganese ions, the Mn3s spectrum is split due to the exchange coupling between the Mn 3s hole and Mn 3d electrons.[31] In first approximation, the magnitude of the exchange splitting is proportional to the local spin of the 3d electrons in the ground state following the expression: $\Delta E \sim (2S+1)$.[31-33] Thus, the magnitude of the 3s exchange splitting allows unequivocal assignment of the oxidation state of the manganese ions: for Mn^{2+}, Mn^{3+} and Mn^{4+} with S=5/2, S=2 and S=3/2 the expected values of Mn3s splitting should be 6 eV, 5eV and 4 eV, respectively. For the reference Mn^{4+} in $LiNi_{0.5}Mn_{0.5}O_2$, the experimentally observed splitting of Mn 3s is 4.7 eV (Table 2). In comparison with the reference Mn^{4+}, the Mn 3s spectra of NM050 and NM067 display a splitting of about 4.5 eV. This indicates clearly that the Mn ions in sodium deficient oxides adopt the oxidation state of 4+ only.

In the energy region of nickel, the XPS spectra of NM050 and NM067 display a major asymmetric peak with a satellite due to Ni 2p3/2. The binding energies are slightly higher in comparison with that of the reference Ni^{2+} in $LiNi_{0.5}Mn_{0.5}O_2$ (Table 2), but they are significantly lower than that typical of Ni^{3+}. For the sake of comparison, Table 2 shows also the binding energies for a reference Ni^{3+} stabilized in layered $LiNi_{0.8}Co_{0.2}O_2$. As one can see, the positions of the asymmetric peak and the satellite increase with about 1 eV when going from Ni^{2+} to Ni^{3+} ions. The comparison suggests that the Ni ions in $Na_xNi_{0.5}Mn_{0.5}O_2$ are in an oxidation state that is intermediate between +2 and +3. However,

Table 2 Mn 3s, Mn $2p_{3/2}$, Mn $2p_{1/2}$, Ni $2p_{3/2}$ and satellite, Ni 3p, Li 1s, Na 2s and Na 1s binding energies for pristine NNM0.5 and NNM0.67 and $Na_xNi_{0.5}Mn_{0.5}O_2$ electrodes after the first discharge, after the first charge and after 8 cycles and stopped at 2.5 V. Data for $LiNi_{0.5}Mn_{0.5}O_2$ and $LiNi_{0.8}Co_{0.2}O_2$ reference materials are also given.

Samples	Mn 3s, eV	Mn 3s, eV	Δ_{Mn3s}, eV	$Mn2p_{3/2}$ / $Mn2p_{1/2}$, eV	Ni $2p_{3/2}$ eV	Ni $2p_{3/2}$ satelite, eV	Ni 3p, eV	Li 1s, eV	Na 2s, eV	Na 1s, eV
NNM 0.50	84.1	88.6	4.5	642.3 / 653.6	854.6	860.8	67.1	-	62.3	1070.4
NNM 0.67	84.6	89.3	4.6	642.6 / 653.7	855.1	860.8	67.6	-	62.5	1070.6
$LiNi_{0.5}Mn_{0.5}O_2$	84.0	88.7	4.7	642.3 / 653.7	854.4	860.5	66.8	53.5		
$LiNi_{0.8}Co_{0.2}O_2$					855.4	861.4				
NM0.67-electrode				642.6 / 653.8	855.8			-	63.8	1072.1
NM0.67 – stopped at 2.5V				642.1 / 653.3	855.7			55.9	64.9	1073.1
NM0.67 – stopped at 4.6V				642.6 / 653.9	856.5 / 854.1			56.7	64.6	1072.7
NM0.67 – 8 cycles stopped at 2.5V				641.9 / 653.1	856.5 / 854.1			55.5	64.0	1072.7

taking into account the multiplet structure of Ni 2p3/2,[31] the assignment of nickel oxidation states based on single binding energy values alone may introduce significant uncertainty.

To check the oxidation state of Ni ions, Table 2 gives also the binding energies of the Ni 3p state. It is obvious that the binding energies of Ni 3p for NM050 and NM067 compositions are higher than that of a reference Ni^{2+} in $LiNi_{0.5}Mn_{0.5}O_2$. It is of importance that the trend to higher binding energies for nickel ions in sodium deficient oxides is more pronounced in the case of Ni 3p state in comparison with the Ni 2p3/2 state, thus revealing a different oxidation state of Ni ions in sodium and lithium oxide analogues. Therefore, both Ni 2p3/2 and Ni 3p data can be interpreted by appearance of Ni ions in both +2 and +3 oxidation states in sodium deficient oxides. The occurrence of Ni^{2+} in $Na_xNi_{0.5}Mn_{0.5}O_2$ can also be related with an impurity of NiO detected by X-ray powder diffraction. In general, the oxidation state of Ni ions is higher than +2 in sodium deficient oxides, while the oxidation state of Mn ions is +4.

The sodium-induced changes in the oxidation state of transition metal ions are further monitored by EPR spectroscopy. While XPS probes the top surface layer (no more than 2 nm), EPR spectroscopy allows analyzing the volume of the particles. When Ni^{2+} and Mn^{4+} occur simultaneously in layered oxides with composition $Li[Li_{(1-2x)/3}Ni_xMn_{(2-x)/3}]O_2$, an EPR response from Mn^{4+} ions has only been detected, while Ni^{2+} ions remain EPR silent.[34,35] However, the presence of Ni^{2+} ions has an impact on the *g*-factor value and line width of Mn^{4+} ions. It is found that the *g*-value for Mn^{4+} increases in a discrete way with the number of Ni^{2+} ions included in its first metal coordination sphere.[34] In the same sequence, the EPR signal from Mn^{4+} becomes broader. The distribution of Ni^{2+} and Mn^{4+} ions inside the layers has a further effect on the EPR line width, but this effect is smaller in comparison with the contribution due to the nickel amount.[36] The EPR line width and the *g*-value of Mn^{4+} depend also on the oxidation state of Ni ions. [11,35] This dependence is demonstrated in case of $LiNi_{0.5}Mn_{0.5}O_2$ analogues obtained by electrochemical delithiation (Fig. 4). Based on X-ray absorption spectroscopy, it has been reported that, during the delithiation of $LiNi_{0.5}Mn_{0.5}O_2$, manganese is electrochemically inactive and remains as Mn^{4+}, whereas the nickel is being oxidized from Ni^{2+} to almost Ni^{4+} through an intermediate state of Ni^{3+}.[37] While Ni^{3+} ions are paramagnetic with S=1/2, Ni^{4+} ions are diamagnetic with S=0. However, the EPR results reveals that the oxidation of Ni^{2+} ions leads to a strong line broadening, accompanied by a decrease in the *g*-value.[35] For completely delithiated oxides containing only paramagnetic Mn^{4+} and diamagnetic Ni^{4+} ions, the g-factor tends to approach that of pure Mn^{4+}.[11,35,38] These results give evidence for a stronger effect of electrochemically generated Ni^{3+} and Ni^{4+} ions on the EPR line width of Mn^{4+} in comparison with that of pristine Ni^{2+} ions. The stronger effect of highly oxidized Ni ions on the EPR parameters of Mn^{4+} can be used to analyze the oxidation state of Ni ions in sodium deficient $Na_xNi_{0.5}Mn_{0.5}O_2$ oxides.

Figure 4 shows the EPR spectra of NM050 and NM067. All spectra consist of a single Lorentzian line with *g*-value of 2.02, which can be attributed to Mn^{4+} ions, as in the case of lithium analogues. The EPR line width slightly increases upon decreasing the nominal Na content, while the *g*-value is not changed. The sodium-induced change in the EPR line width of Mn^{4+} can be explained by a corresponding variation in the oxidation state of nickel ions. To rationalize this dependence, the EPR line widths and the g-values for sodium deficient oxides are compared with those for electrochemically delithiated lithium oxides. The comparison indicates that the oxides having the same sodium and lithium content display similar EPR line widths of Mn^{4+}. On the one hand, the EPR results reveal that sodium deficiency in $Na_xNi_{0.5}Mn_{0.5}O_2$ is compensated by the occurrence of highly oxidized nickel ions. On the other hand, EPR results confirm the correctness of the determination of the sodium content in $Na_xNi_{0.5}Mn_{0.5}O_2$ by the Rietveld refinement method.

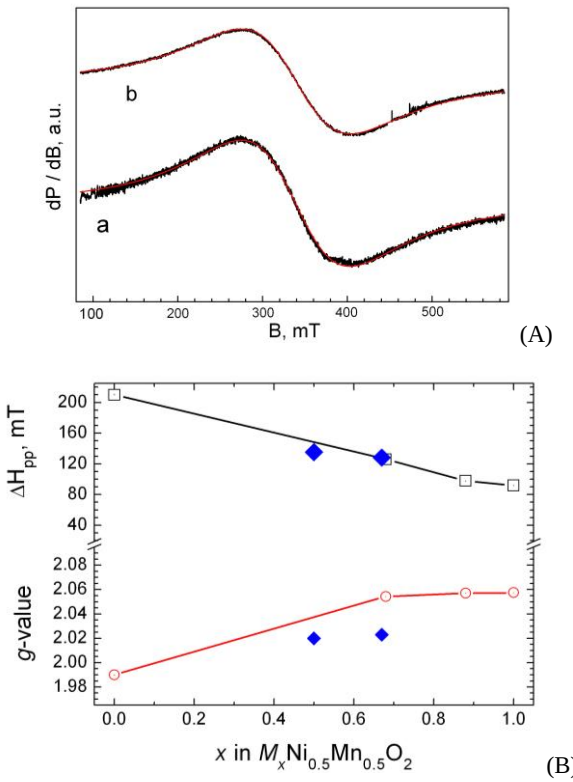

Figure 4 (A) EPR spectra for NM050 (a) and NM067 (b). (B) EPR line width (ΔH_{pp}) and g-factor for NM050 and NM067 (diamonds). For the sake of comparison, the effect of highly oxidized nickel ions on the EPR line width and g-factor for Mn^{4+} in $Li_xNi_{0.5}Mn_{0.5}O_2$ are also presented (blank symbols).

The *g*-factor of Mn^{4+} in sodium deficient oxides has lower value in comparison with that for lithium oxides. This reflects the different nature of Mn-O bonding in both sodium and lithium oxides. The lower values for g-factor imply the formation of more covalent Mn-O bonds in $Na_xNi_{0.5}Mn_{0.5}O_2$ oxides. The EPR results are in agreement with the bond lengths determined by X-ray structural analysis. In sodium deficient oxides, the transition metal ions form shorter bond with oxygen compared to that in delithiated oxides: mean $Ni_{0.5}Mn_{0.5}$-O bond lengths of 1.91 Å and 1.94 Å for $Na_xNi_{0.5}Mn_{0.5}O_2$ with x=0.67 and $Li_xNi_{0.5}Mn_{0.5}O_2$ with 0.6<x<0.7, respectively.[39]

Electrochemical intercalation of Li^+ with $Na_xNi_{0.5}Mn_{0.5}O_2$

Recently we have demonstrated that the ability of sodium deficient oxides to participate in ion exchange reactions with

lithium determines their potential for direct use as positive electrodes in lithium ion batteries. Figure 5 shows the first discharge curves for oxides with nominal sodium content varying between 0.5 and 1.0. For better comparison of the electrochemical characteristics of all oxides, the same Figure gives also the capacity-voltage curves as first derivatives.

For the first discharge, the capacity decreases from 112 to 78 mAh/g upon increasing the nominal sodium content from Na/(Ni+Mn)=0.5 to Na/(Ni+Mn)=0.67, reaching a nearly constant value of about 75 mAh/g for Na/(Ni+Mn)>0.67 (Fig. 5). All oxides deliver the capacity in two potential steps: between 3.9 and 3.4 V and between of 3.2 and 2.9 V, respectively. In addition, the oxide with a nominal ratio of Na-to-(Ni+Mn)=0.5 displays an additional less intensive peak at about 2.7 V. The comparison of the discharge curves indicates that the capacity associated with the higher voltage range decreases with the nominal sodium content, while the lower-voltage peak displays a capacity that appears to be insensitive towards the nominal sodium content. Based on the electrochemical properties of lithium nickel manganese oxides,[1,2] the two peaks at high and low potentials can be attributed to the consecutive reduction of nickel and manganese ions. It seems that the oxidation state of the nickel ions depends on the sodium content, while the manganese ions acquire constant oxidation state in all $Na_xMn_{1/2}Ni_{1/2}O_2$ compositions. This result is in good agreement with the data from XPS analysis on the oxidation state of Ni and Mn ions in $Na_xNi_{0.5}Mn_{0.5}O_2$ (Fig. 3).

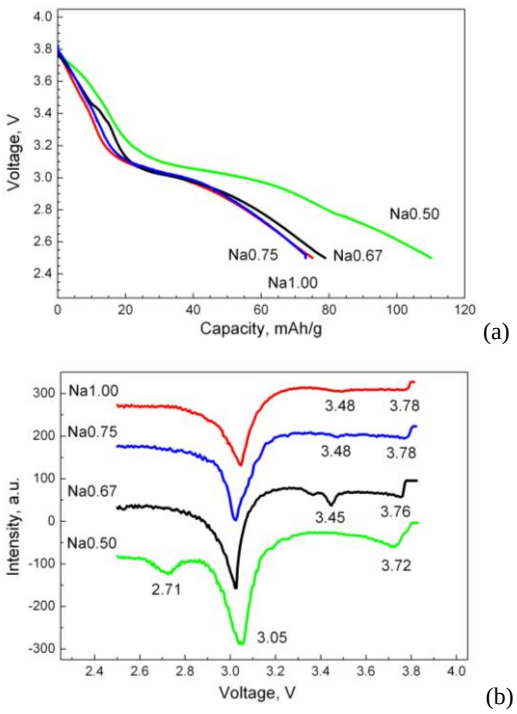

Figure 5 First discharge of $Na_xNi_{0.5}Mn_{0.5}O_2$ with a nominal sodium contents of 0.5, 0.67, 0.75 and 1.0 (a). Discharge curves as first derivatives are also shown (b). The current rate is C/100.

The observed variations in the shape of the first discharge curve and the discharge capacity provide evidence for the sodium induced changes in the oxidation state of transition metal ions in $Na_xMn_{1/2}Ni_{1/2}O_2$. Assuming lack of side redox reactions, the first discharge capacity can serve as a measure for the average oxidation state of transition metal ions. Table 1 shows the calculated amount of intercalated Li^+ per formula unit $Na_xNi_{0.5}Mn_{0.5}O_2$, as well as the corresponding oxidation state of the transition metal ions. Two features can be outlined. First, all oxides intercalate lithium in amounts lower than 0.5 mole, which compensates for sodium deficiency in $Na_xNi_{0.5}Mn_{0.5}O_2$. It is generally accepted that the Na content and the requirement for charge neutrality yield the average oxidation state of the transition metal ions in Na_xMO_2 oxides. The comparison shows that the oxidation state of the transition metal ions, determined by electrochemical intercalation of Li is in good agreement with the expected values for a structure formula $Na_xNi_{0.5}Mn_{0.5}O_2$ (Table 1). Second, the oxides $Na_xNi_{0.5}Mn_{0.5}O_2$ with x=0.75 and x=1.0 display the same amount of intercalated lithium (about 0.3 mole of Li^+), thus indicating a limited solubility of sodium in $Na_xNi_{0.5}Mn_{0.5}O_2$, which reaches a value of about 0.7 mole.

During the reverse process of charging, the two peaks at 3.1 and 3.8 V are clearly resolved for all oxides (Fig. 6). The charge capacity is extremely sensitive to the upper voltage limit. By extending the upper voltage limit from 4.4 to 4.6 V, the charge capacity increases from 160 up to 320 mAh/g. This outlines that more than 0.7 mole of Li is extracted after the first charge. The observed trend is valid for oxides having different sodium amount. An important issue is that the first charge capacity exceeds the corresponding discharge capacity even when the upper voltage limit is restricted to 4.4 V (Fig. 6). This means that lithium together with sodium is extracted from the oxide during the first charge process. In addition, a partial exchange of Na^+ with Li^+ can not be rejected. To analyze the processes of Li^+/Na^+ deintercalation and exchange, Table 3 gives the chemical compositions of electrodes determined by LA-ICPMS. After the first discharge up to 2.5 V (i.e. after Li intercalation), there is a strong increase in the Li-to-Na ratio, which reveals a lowering of the sodium content in the electrodes in comparison with the pristine compositions (Table 3). The extraction of Li^+ ions during the charge process up to 4.6 V is manifested by a consecutive decrease in the Li-to-Na ratio (Table 3). The observed changes in the Li-to-Na ratio imply that partial Li^+/Na^+ exchange reactions starts to develop at the beginning of the Li intercalation (Table 3). Contrary to lithium and sodium, the nickel and manganese content remains constant during the electrochemical reaction (Table 3).

The dramatic increase in the charge capacity above 4.5 V is related with the development of a new peak, especially for oxides with nominal Na-(Ni+Mn) ratio higher than 0.7 (Fig. 6). The high-voltage oxidation peak is not recovered during the reverse reduction process and it represents the main reason for the irreversibility of electrochemical lithium reaction for $Na_xNi_{0.5}Mn_{0.5}O_2$. The irreversibility reaches a higher value (of about 260 mAh/g) for $Na_xNi_{0.5}Mn_{0.5}O_2$ with a nominal sodium content of 1.0. At a first glance, the observed capacity loss could be associated with the sodium carbonate present as an impurity in $Na_xNi_{0.5}Mn_{0.5}O_2$ compositions with a nominal sodium content higher than 0.70. However, the occurrence of additional side reactions above 4.4 V between the electrode and the electrolyte cannot be excluded.

Stable electrochemical performance is achieved after several

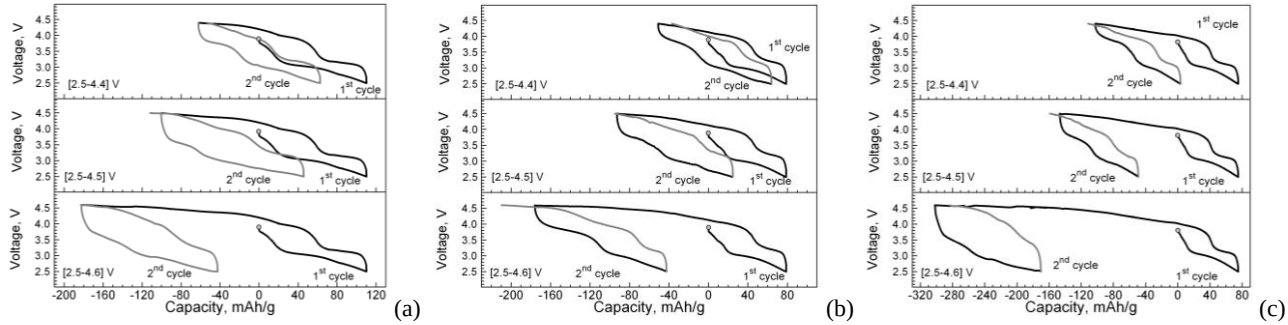

Figure 6 First and second charge/discharge curves for $Na_xNi_{0.5}Mn_{0.5}O_2$ with nominal sodium contents of 0.5 (a), 0.67 (b) and 1.0 (c).

cycles. Figure 7 gives the charge/discharge curves after 5 cycles. When the electrochemical reaction takes place within a limited potential range (2.5 – 4.4 V), both charge and discharge curves display two plateau - at 3.8 and 3.1 V, respectively. The two peaks become less pronounced, when the electrochemical reaction proceeds within a wider potential range (Fig. 7). It is noticeable that the coulombic efficiency increases and tends to reach 99% after 5 cycles. A stable capacity of about 120 - 130 mAh/g is reached when NM067 is cycled between 2.5-4.6 V, while for NM050 the same reversible capacity is attained within the potential range of 2.5-4.5 V. This means that the electrochemical reaction takes place through reversible intercalation of 0.5-0.6 mole of Li in the oxides with different nominal sodium content. The sodium content in cycled electrodes (i.e. 8 cycles between 2.5 and 4.6 V) is lower than that in the pristine compositions and it is comparable with that for the electrode after the first discharge to 2.5 V (Table 3). This reveals that a partial exchange of sodium with lithium is occurring mainly during the first discharge. It is of importance that the sodium extraction and sodium exchange reactions unify the properties of $Na_xNi_{0.5}Mn_{0.5}O_2$ electrodes, irrespective of their pristine compositions. On the other hand, the appearance of sodium in the cycled compositions contributes to the structure stability of electrodes during the electrochemical reaction. After prolonged cycling the Ni-to-Mn ratio seems unchanged (Table 3). In summary, one can explain the electrochemical reaction by participation of delithiated $Li_{(0.3-0.2)}Na_{(0.1-0.2)}Ni_{0.5}Mn_{0.5}O_2$ and lithiated $Li_{(0.9-0.8)}Na_{(0.1-0.2)}Ni_{0.5}Mn_{0.5}O_2$ compositions. The suggested formula, where both Li^+ and Na^+ occur in the interlayer space, can be understood on the basis of the available crystallographic data in the literature. As a good example it deserves mentioning the layered cobaltate with a composition $Li_{\sim0.42}Na_{\sim0.37}CoO_2$.[40-42] The structure of $Li_{\sim0.42}Na_{\sim0.37}CoO_2$ consists of two alternative AO_2 blocks: a *P2*-type sodium block and an *O3*-type lithium one.[40-42] Contrary to $Li_{\sim0.42}Na_{\sim0.37}CoO_2$, the incorporation of Li into *O3*-$NaNi_{0.5}Mn_{0.5}O_2$ has recently been shown to proceed by the formation of a *P2/O3* intergrowth at an atomic scale.[43] In analogy, the supposed structure of mixed Na^+/Li^+-nickel-manganese oxides could be described as composed of *P3* and *O3*-type of domains. The stability of the domain structure of the mixed Na^+/Li^+-nickel-manganese oxides can be understood, if we take into account the data of Ceder *et al.* on the structural transformation of *O3*-type of Na and Li layered compounds during alkali deintercalation.[44] Based on first principle calculations, it has been established that for $Li_{0.5}MO_2$ and $Na_{0.5}MO_2$ all Li compounds strongly favor a spinel structure, while this driving force does not exist in case of layered Na compounds.[44] The last statement is also valid for the Na compounds with a layered *P3*-type structure, since the highly unfavorable prismatic sites inhibit the transition metal migration through the Na layer.[44]

The two-stage intercalation reactions, associated with high and low-voltage plateaus, are clearly distinguished even when the high charge/discharge rates are applied (Fig. 8a). As it was expected, the first discharge capacity slightly decreases: from 78 mAh/g for a C/100 (Fig. 5) rate to 52 mAh/g for a C/20 rate (Fig. 8a). However, the capacity shown during numerous cycles is quite good: about 85-95 mAh/g, which corresponds to a reversible intercalation of about 0.4 mole Li per formula unit (Fig. 8b).

The two-stage intercalation reaction is a specific for $Na_xNi_{0.5}Mn_{0.5}O_2$. Figure 8c compares the first derivatives of the charge/discharge curves in the potential range of 2.5-4.5 V for both sodium and lithium nickel manganese oxides. In accordance with previous studies, the lithium analogue displays one-stage reaction with oxidation and reduction peaks at 3.8 and 3.70 V, respectively.[7,9,11] The lithium intercalation in $LiNi_{0.5}Mn_{0.5}O_2$ proceeds thanks to the redox properties of nickel ions (i.e. redox couples Ni^{2+}/Ni^{4+}), while Mn^{4+} remain inactive.[7,9,11] In comparison with $LiNi_{0.5}Mn_{0.5}O_2$, $Na_xNi_{0.5}Mn_{0.5}O_2$ displays an

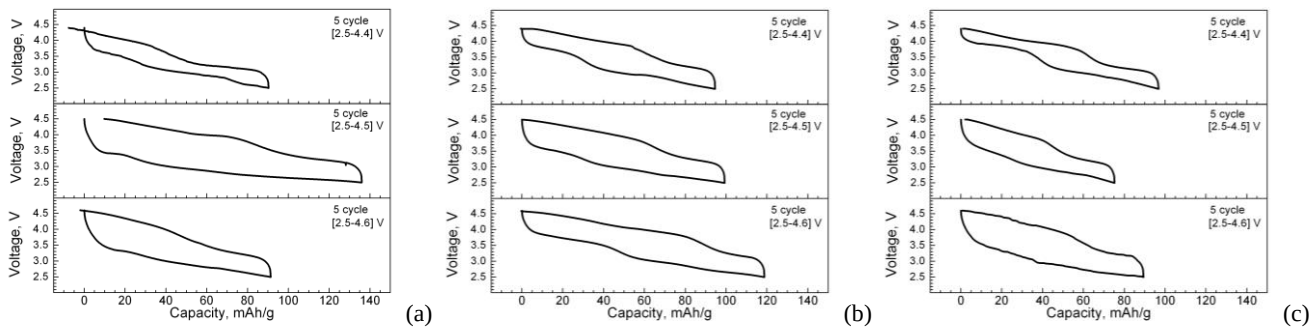

Figure 7 The charge/discharge curves after the 5 cycles for $Na_xNi_{0.5}Mn_{0.5}O_2$ with nominal sodium contents of 0.5 (a), 0.67 (b) and 1.0 (c).

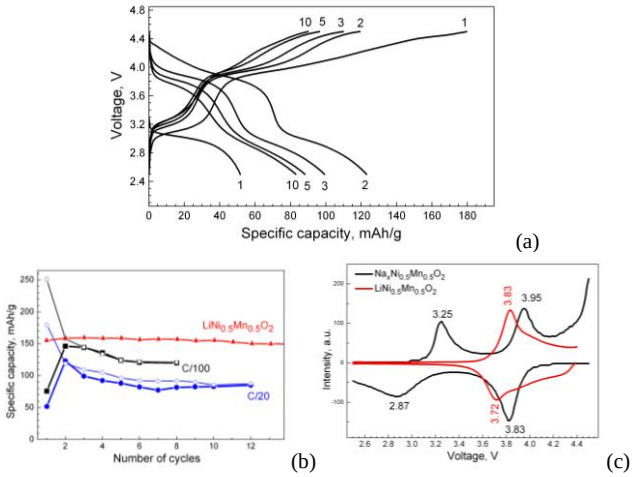

Figure 8 (a) Charge/discharge curves of $Na_{0.67}Ni_{0.5}Mn_{0.5}O_2$ at a rate of C/20 for 1, 5 and 10 cycles. The cell starts with a discharge mode. (b) Cycling stability curves for $Na_{0.67}Ni_{0.5}Mn_{0.5}O_2$ (black and blue lines at C/100 and C/20 rates) and $LiNi_{0.5}Mn_{0.5}O_2$ (red line at a C/20 rate). Full and open symbols correspond to the discharge and charge capacities, respectively. (c) Discharge/charge curves as first derivatives after 5 cycles for $Na_{0.67}Ni_{0.5}Mn_{0.5}O_2$ (black lines) and $LiNi_{0.5}Mn_{0.5}O_2$ (red lines).

additional plateau at 3.1 V, which is most probably related with the redox properties of the Mn ions (XPS data, Figure 3). In addition, $LiNi_{0.5}Mn_{0.5}O_2$ delivers between 2.5 and 4.4 V a higher capacity in comparison with that for $Na_xNi_{0.5}Mn_{0.5}O_2$ (Fig. 8c). The cycling stability of $LiNi_{0.5}Mn_{0.5}O_2$ is also better (Fig. 8c). It is worth mentioning that for the comparative analysis we have selected $LiNi_{0.5}Mn_{0.5}O_2$ having the best electrochemical properties due to its optimized morphology and cationic distribution.[11] In this respect, the electrochemical performance of $Na_xNi_{0.5}Mn_{0.5}O_2$ is not optimized. The coulombic efficiency for $Na_xNi_{0.5}Mn_{0.5}O_2$ increases during cycling (Fig. 8b). It appears that after several cycles the efficiency becomes more than 98 % depending on the rate of charge/discharge.

Surface composition of $Na_xMn_{1/2}Ni_{1/2}O_2$electrodes

Contrary to the lithium analogues, sodium deficient nickel manganese oxides display high reactivity towards the electrolyte consisting of ethylene carbonate/diethyl carbonate and $NaPF_6$ salt.[45] Based on accelerating rate calorimetry, Dahn et al. [45] have found out that desodiated $Na_xNi_{0.5}Mn_{0.5}O_2$ reacts with the PVDF binder forming NaF and transition metal oxides at temperatures above 175°C. The reaction between $Na_{0.5}Ni_{0.5}Mn_{0.5}O_2$ and $NaPF_6$ EC:DEC has been shown to produce additional products such as $Na_3(Ni,Mn)F_6$ and $Na(Ni,Mn)F_3$.[45]

As all the electrodes were prepared by mixing of $Na_xNi_{0.5}Mn_{0.5}O_2$ with the PVDF binder and carbonaceous additives, an important issue is whether $Na_xNi_{0.5}Mn_{0.5}O_2$ is stable towards PVDF prior to the electrochemical reaction. The XPS spectra show that the binding energies of Na1s and Na2s are shifted with more than 1 eV, when going from the pristine powder to the electrode mixture, while the binding energies of Ni2p3/2 and Mn2p3/2 are practically unchanged (Table 2). The strongly shifted Na1s and Na 2s peaks fall within the range, where the binding energies for Na in NaF occur at 1072 eV for Na1s [46] and 63 eV for Na2s, respectively. Therefore, the two peaks due to Na1s and Na2s in the $Na_{0.67}Ni_{0.5}Mn_{0.5}O_2$ electrode can be assigned to NaF. This means that the sodium deficient $Na_{0.67}Ni_{0.5}Mn_{0.5}O_2$ oxide is reacting with the PVDF binder during the electrode fabrication forming NaF. The reaction is developing on the oxide surface since the XRD pattern of $Na_{0.67}Ni_{0.5}Mn_{0.5}O_2$ in the electrode mixture remains unchanged. The surface Mn-to-Ni ratio seems to remains constant during the electrode preparation and tends to that value, determined by chemical analysis (Table 3).

The formation of surface NaF is further confirmed by the F1s spectrum (Fig. 9). There are two overlapping signals with binding energies at 688.1 and 685.2 eV. The relative intensities of the high and low energy signals are 0.76 to 0.23, respectively. The high-energy peak (i.e. at 688.1 eV) is associated with fluorine atoms in PVDF binder,[47] while the low-energy peak (i.e. 685.2 eV) corresponds to fluoride ion in NaF.[48]

To understand the lithium intercalation process into *P3*-$Na_xNi_{0.5}Mn_{0.5}O_2$ oxides we have also examined the surface changes of the electrode materials during the electrochemical reaction by means of XPS. Three types of electrode samples were studied: $Na_{0.67}Ni_{0.5}Mn_{0.5}O_2$ after the first discharge to 2.5 V, $Na_{0.67}Ni_{0.5}Mn_{0.5}O_2$ after the first charge to 4.6 V, and $Na_{0.67}Ni_{0.5}Mn_{0.5}O_2$ after the 8 cycles between 2.5 and 4.6 V and stopped at 2.5 V. The composition of the surface film is identified by XPS. Figures 3 and 9 compare the XPS spectra of pristine $Na_{0.67}Ni_{0.5}Mn_{0.5}O_2$ and $Na_{0.67}Ni_{0.5}Mn_{0.5}O_2$ electrodes in the energy region characteristic of manganese, nickel, sodium, lithium, fluorine and phosphorus.

After the first discharge to 2.5 V, the centre of gravity of the asymmetric peak due to Mn 2p3/2 displays a positive shift, while the Ni 2p3/2 peak does not undergo any significant changes (Fig. 3). The reverse process of charging up to 4.6 V leads to a restoration of the binding energy of Mn 2p3/2 and to a split of the

Table 3 Chemical and surface composition of $Na_xNi_{0.5}Mn_{0.5}O_2$ electrode and $Na_xNi_{0.5}Mn_{0.5}O_2$ electrode after the first discharge, after the first charge and after 8 cycles and stopped at 2.5 V. Data are determined based on chemical and XPS analysis (CA and XPS, respectively).

Initial *x* in $Na_xNi_{0.5}Mn_{0.5}O_2$	Mn/Ni (CA)	Mn/Ni (XPS)	Na1s/Na2s (XPS)	Li/Na (CA)	Li1s/Na2s (XPS)	F1s / P2p (XPS)	XPS: relative part of F1s (685) / F1s(688)
NaNM0.67-electrode	1.15	1.08	2.0	0	0	-	0.23 / 0.76
NaNM0.67 – stopped at 2.5V	1.18	0.93	2.1	6.75	4.2	3.1	0.41 / 0.59
NaNM0.67 – stopped at 4.6V	1.17	0.94	1.8	3.61	2.2	6.6	0.70 / 0.30
NaNM0.67 – 8 cycles stopped at 2.5V	1.18	0.98	1.8	6.70	3.0	7.0	0.44 / 0.56

Ni 2p3/2 peak into two components at 856.5 and 854.1 eV (Fig. 3). The Mn2p3/2 and Ni2p3/2 spectra of the cycled electrode seem similar to that of the electrode obtained after the first discharge to 2.5 V (Table 2). The surface Mn-to-Ni ratio is close to that of the pristine oxide (Table 3). It is worth mentioning that the bulk phase Mn-to-Ni ratio determined by chemical analysis remains also constant (Table 3).

As a general trend, the increase in the binding energy is usually used as a criterion for the changes of the formal valence state of Mn and Ni ions. For example, the binding energy for Mn^{4+} ions in MnO_2 is higher than that for Mn^{3+} in Mn_2O_3: 642.6 eV and 641.9 eV, respectively.[27,49,50] The same picture is observed for nickel ions: the binding energy for Ni^{3+} in $LiNiO_2$ is 656.0 eV compared to 654.8 eV for Ni^{2+} in NiO.[51,52] Therefore, we can assign the observed increase in the binding energy of Mn2p3/2 during the first discharge to a reduction of Mn^{4+} to Mn^{3+} ions, while both Ni^{3+} and Ni^{2+} ions contribute to the XPS profile of the oxide charged to 4.6 V. Based on the XPS data, it appears that lithium intercalation within the 3.1 V-range proceeds at the expense of the reduction of Mn^{4+} to Mn^{3+}. During the reverse process of alkaline ion extraction, both manganese and nickel ions are being oxidized. However, even at 4.6V some unreacted Ni^{2+} ions are still available. The presence of these ions can be related with the impurity NiO phase, which does not take part in the electrochemical reaction. It is of importance that both the oxidation and reduction processes are reversible.

The XPS spectra in the energy region characteristic of Na and Li elements reflect more clearly the electrochemical reaction of reversible lithium intercalation in $Na_{0.67}Ni_{0.5}Mn_{0.5}O_2$ (Fig. 9). For surface analysis, we used both Na1s and Na2s spectra in order to probe different sampling depth: Na1s provides information about the few top surface layers only, while Na2s signal can be regarded as more "bulk-like". In addition, the electron energy for Na2s falls within the range where the electron energy for Li1s appears. This means that the surface sensitivity for Na2s and Li1s is similar. In the energy region of Na1s and Na2s, cycled electrode compositions display broad signals with binding energies varying between 1072 and 1073 eV and 63.8 and 64.9 eV, respectively (Fig. 9, Table 2). The binding energies for both Na1s and Na2s signals allow assigning them to NaF. This reveals that NaF is spread over the surface of $Na_{0.67}Ni_{0.5}Mn_{0.5}O_2$ electrode and it is stable during the electrochemical reaction.

When $Na_{0.67}Ni_{0.5}Mn_{0.5}O_2$ is discharged to 2.5 V, a signal due to Li1s grows up in intensity (Fig. 9). The appearance of the Li1s signal gives clear evidence for interaction of Li^+ with $Na_{0.67}Ni_{0.5}Mn_{0.5}O_2$. The binding energy of Li1s is about 55.5 eV, which is typical of LiF. For the sake of comparison, the binding energy of Li1s in $LiNi_{0.5}Mn_{0.5}O_2$ is 53.5 eV, i.e. with 2 eV lower than that for LiF (Table 2). During the electrochemical reaction, the binding energy of Li1s is changing simultaneously with that of Na2s (Table 2). The XPS results demonstrate a deposition of LiF on $Na_{0.67}Ni_{0.5}Mn_{0.5}O_2$ in addition to NaF. The surface ratio of Li-to-Na calculated from Li1s and Na2s is higher than 3, which is indicating an enrichment of $Na_{0.67}Ni_{0.5}Mn_{0.5}O_2$ surface in LiF (Table 3). It appears that LiF is deposited immediately after the first discharge and it is remaining stable during the cell cycling. The surface Li-to-Na ratio of cycled electrodes follows the trend of changes in the bulk Li-to-Na ratio determined by LA-ICPMS (Table 3).

The F 1s and P 2p spectra display the pronounced changes occurring on the surface of oxides (Fig. 9). As in the case of the electrode mixture, two overlapping signals give rise to the profile of the F 1s spectrum for all discharged and charged electrodes. The binding energy of the high-energy peak slightly decreases from 688.1 to 687.2 eV, when going from the pristine to the cycled electrodes, while the low-energy peak increases in the same order of magnitude: from 685.2 to 686.6 eV. The parameter that is strongly changed during the electrochemical reaction is the relative intensity of the two signals (Table 3). After the first lithiation of $Na_xNi_{0.5}Mn_{0.5}O_2$, the intensity of the low energy signal increases at the expense of the high energy signal (Fig. 9, Table 3). During the reverse process of lithium extraction, there is a further increase in the relative intensity of the low energy signal reaching a maximum value of 0.7. It is noticeable that the observed changes in the relative intensity are reversible: after 8 cycles the relative intensity of the low energy peak tends to reach

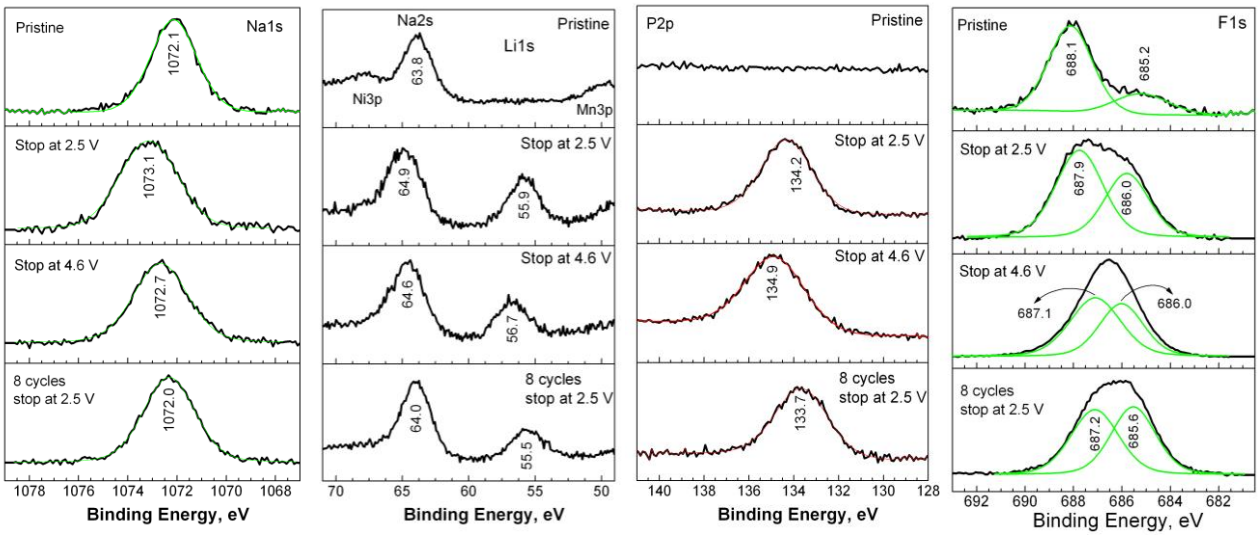

Figure 9 XPS spectra in the Na1s, Na 2s, Li 1s, P 2p and F 1s regions for pristine NM067 electrode and their counterparts after the electrochemical reaction.

that of $Na_xNi_{0.5}Mn_{0.5}O_2$ obtained after the first discharge (Table 3). The F 1s peak with a binding energy varying between 685 and 686 eV can be related with fluoride-based compounds such as LiF and NaF,[53,48] while the F 1s peak centred in the range of 687-688 eV are associated with fluorine-based compounds such as $Li_xPF_yO_z$ and Li_xPF_y.[54-56]

The P 2p spectrum displays one broad peak, whose centre of gravity depends on whether a lithiation or a delithiation process is taking place (Fig. 9): 134.2 eV and 134.9 eV for NM067 discharged to 2.5 V and charged to 4.6 V, respectively. According to the literature data, the peak with the lower binding energy (i.e. at <134.5 eV) is usually associated with P_2O_5 and/or $Li_xPF_yO_z$, while the peak at >134.5 eV – with Li_xPF_y.[54,56,57] Taking into account these data, one can identify P_2O_5 and/or $Li_xPF_yO_z$ compounds on the surface of the lithiated oxide, while Li_xPF_y is mainly adsorbed on the surface of the delithiated oxide. The formation of the surface film is a reversible process: the surface composition becomes again rich in P_2O_5 and/or $Li_xPF_yO_z$ compounds when the cell is discharged 8 times to 2.5 V (Fig. 9). The appearance of surface Li_xPF_y and/or Na_xPF_y compounds can explain the observed variation in the binding energies of both Li1s and Na2s for $Na_xNi_{0.5}Mn_{0.5}O_2$ electrodes. The surface P-to-F ratio confirms once again the formation of an interphase richer in Li_xPF_y and/or Na_xPF_y compounds.

The occurrence of fluorine-based compounds on the electrode surfaces is a well established phenomenon for lithium transition metal oxides, when they are in contact with a $LiPF_6$-based electrolyte.[58] The thermal instability of $LiPF_6$ determines its high reactivity towards surface oxides. $LiPF_6$ has been shown to decompose into LiF and PF_5 even at room temperature. The reaction product PF_5 is a strong Lewis acid and it plays a crucial role in the formation of the solid electrolyte interphase layer that is composed of mixed organic and inorganic compounds. It appears that the same mechanism acts in the case of sodium deficient oxides.

Conclusions

Freeze-dried acetate precursors with nominal Na-to-(Ni+Mn) ratio varying between 0.5 and 1.0 yield at 700 °C sodium deficient nickel manganese oxides $Na_xNi_{0.5}Mn_{0.5}O_2$ with a layered *P3*-type of structure, where the sodium content is restricted between 0.5 and 0.75 mole ($0.5 \le x < 0.75$). In addition, impurities including NiO and Na_2CO_3 phases are also detected. At 700 °C, $Na_xNi_{0.5}Mn_{0.5}O_2$ consists of flat thin particles with dimensions covering a broad size range from 20 to 160 nm. Some of the particles with sizes higher than 100 nm display a trigonal superstructure, which is dependent on the sodium content. In $Na_xNi_{0.5}Mn_{0.5}O_2$, manganese ions appear in their usual oxidation state of +4, while the oxidation state of nickel ions is higher than +2 and it depends also on the sodium content.

Sodium deficient nickel manganese oxides $Na_xNi_{0.5}Mn_{0.5}O_2$ react with PVDF, which was used as a binder for the electrode preparation. As a result, the surface of $Na_xNi_{0.5}Mn_{0.5}O_2$ is covered with NaF, while the bulk phase remains intact. During the first discharge, the electrochemical reaction is taking place through simultaneous Li^+ intercalation and Li^+/Na^+ exchange. The intercalation of Li^+ is developing in two potential ranges at 3.1 and 3.8 V at the expense of the consecutive reduction of highly oxidized nickel and manganese ions. During the reverse charge process, both Li^+ and Na^+ deintercalation is taking place. The reactions of intercalation and ionic exchange unify the properties of $Na_xNi_{0.5}Mn_{0.5}O_2$ electrodes regardless of their pristine compositions. As a result, $Na_xNi_{0.5}Mn_{0.5}O_2$ oxides show reversible capacity of about 120 - 130 mAh/g within the potential range of 2.5-4.5 V. The reaction includes reversible lithium intercalation between delithiated $Li_{(0.3-0.2)}Na_{(0.1-0.2)}Ni_{0.5}Mn_{0.5}O_2$ and lithiated $Li_{(0.9-0.8)}Na_{(0.1-0.2)}Ni_{0.5}Mn_{0.5}O_2$ compositions. The structure of mixed Na^+/Li^+-nickel-manganese oxides could be most probably described as composed of *P3* and *O3*-type of domains.

In the course of the electrochemical reaction, the oxide surface is covered with sodium and lithium phospho-fluorine-based compounds, which remain stable during the cycling. This is a consequence of the reactivity of sodium deficient oxides towards $LiPF_6$ salt in the electrolyte, the reaction being intensified at potentials higher than 4.4 V. Further optimization of the electrochemical properties of sodium deficient oxides are closely related with the selection of appropriate electrolyte composition.

In general, the intercalation properties of sodium deficient nickel manganese oxides open new possibilities for design of low-cost electrode materials for lithium ion batteries.

Acknowledgments

This work was supported by ESF (Grant BG051PO001-3.3.06-0050).

Notes and references

[a] *Institute of General and Inorganic Chemistry, Bulgarian Academy of Sciences, 1113 Sofia, Bulgaria. Fax: +359 2 8705024; Tel: +359 2 979 3915; E-mail: radstoy@svr.igic.bas.bg*
[b] *Institute of Catalysis, Bulgarian Academy of Sciences, 1113 Sofia, Bulgaria.*
[c] *Institute of Mineralogy and Crystallography, Bulgarian Academy of Sciences, 1113 Sofia, Bulgaria.*

1 B.L. Ellis, K.T. Lee and L.F. Nazar, *Chem. Mater.*, 2010, **22**, 691.
2 P. He, H. Yu, D. Li and H. Zhou, *J. Mater. Chem.*, 2012, **22**, 3680.
3 H.J. Orman and P.J. Wiseman, *Acta Crystallogr. C*, 1986, **40**, 123.
4 C. Delmas, C. Fouassier and P. Hagenmuller, *Physica B+C*, 1980, **91**, 81.
5 M.E. Spahr, P. Novák, B. Schnyder, O. Haas and R. Nesper, *J. Electrochem. Soc.*, 1998, **145**, 1113.
6 T. Ohzuku, M. Ariyoshi, Y. Makimura, Y. Yabuuchi and K. Sawai, *Electrochemistry*, 2005, **73**, 2.
7 Z. Lu, L.Y. Beaulieu, R.A. Donaberger, C.L. Thomas and J.R. Dahn, *J. Electrochem. Soc.*, 2002, **149**, A778.
8 J. Reed and G. Ceder, *Electrochem. Solid state Lett.*, 2002, **5**, A145.
9 W.-S. Yoon, C.P. Grey, M. Balasubramanian, X.-Q. Yang and J. McBreen, *Chem. Mater.*, 2003, **15**, 3161.
10 R. Stoyanova, E. Zhecheva, R. Alcántara and J.L. Tirado, *J. Mater. Chem.*, 2006, **16**, 359.
11 M. Yoncheva, R. Stoyanova, E. Zhecheva, R. Alcántara, G. Ortiz, J.L. Tirado, *Electrochim Acta*, 2009, **54**, 1694.
12 Y. Arachi, H. Kobayashi, S. Emura, Y. Nakata,, M. Tanaka and T. Asai, *Chem. Lett.*, 2003, **32**, 60.
13 Y. Koyama, N. Yabuuchi, I. Tanaka, H. Adachi and T. Ohzuku, *J. Electrochem. Soc.*, 2004, **151**, A1545.
14 H.H. Li , N. Yabuuchi , Y.S. Meng , S. Kumar , J. Breger , C.P. Grey and Y. Shao-Horn, *Chem. Mater.*, 2007, **19**, 2551.
15 S. Bach, J.P. Pereira-Ramos and P. Willmann, *Electrochim. Acta*, 2006, **52**, 504.

16 Y. Tang, D. Sun, H. Wang, X. Huang, H. Zhang, S. Liu and Y. Liu, *RSC Adv.*, 2014, **4**, 8328.
17 H. Wang, S. Liu, Y. Ren, W. Wang and A. Tang, *Energy Environ. Sci.*, 2012, **5**, 6173.
18 M. Yoncheva, R. Stoyanova, E. Zhecheva, E. Kuzmanova, M. Sendova-Vassileva, D. Nihtianova, D. Carlier, M. Guignard and C. Delmas, *J. Mater. Chem.* 2012, **22**, 23418.
19 M. Kalapsazova, R. Stoyanova and E. Zhecheva, *J. Solid State Electrochem.*, 2014, **18**, 2343.
20 K. Kang, Y.S. Meng, J. Berger, C.P. Grey and G. Ceder, *Science*, 2006, **311**, 977.
21 J. Cabana, N.A. Chernova, J. Xiao, M. Roppolo, K.A. Aldi, M.S. Whittingham and C.P. Grey, *Inorg. Chem.*, 2013, 52, 8540.
22 S. Komaba, N. Yabuuchi, T. Nakayama, A. Ogata, T. Ishikawa and I. Nakai, *Inorg. Chem.*, 2012, **51**, 6211.
23 Zh. Lu, R. A. Donaberger and J. R. Dahn, *Chem. Mater.*, 2000, **12**, 3583.
24 J.M. Paulsen, R. Donaberger and J.R. Dahn, *Chem. Mater.*, 2000, **12**, 2257.
25 D.H. Lee, J. Xu, Y.S. Meng, *Phys. Chem. Chem. Phys.*, 2013, **15**, 3304.
26 Rodríguez-Carvajal, J. FULLPROF (1990) A Program for Rietveld Refinement and Pattern Matching Analysis. In Abstracts of the Satellite Meeting on Powder Diffraction of the XV Congress of the IUCr, Toulouse, France p 127.
27 Sv. Ivanova, E. Zhecheva, R. Stoyanova, D. Nihtianova, S. Wegner, P. Tzvetkova and Sv. Simova, *J. Phys. Chem. C*, 2011, **115**, 25170.
28 T. A. Platova, I. R. Mukhamedshin, H. Alloul, A. V. Dooglav and G. Collin, *Phys. Rev. B*, 2009, **80**, 224106.
29 F.-T. Huang, M.-W. Chu, G. J. Shu, H. S. Sheu, C. H. Chen, L.-K. Liu, P.A. Lee and F. C. Chou1, *Phys. Rev. B*, 2009, **79**, 014413.
30 R.P. Gupta and S.K. Sen, *Phys Rev. B*, 1975, **12**, 12.
31 V.A.M. Brabers, F.M. van Setten and P.S.A. Knapen, *J. Solid State Chem.*, 1983, **49**, 93.
32 V. R. Galakhov, M. Demeter, S. Bartkowski, M. Neumann, N. A. Ovechkina, E. Z. Kurmaev, N. I. Lobachevskaya, Ya. M. Mukovskii, J. Mitchell, D. L. Ederer, *Phys. Rev. B*, 2002, **65**, 113102.
33 P.S. Bagus, R. Broer and E.S. Ilton, *J. Electron Spectroc. Relat. Phenom.*, 2008, **165**, 46.
34 R. Stoyanova, E. Zhecheva and S. Vassilev, *J. Solid State Chem.*, 2006, **179**, 378.
35 M. Yoncheva, R. Stoyanova, E. Zhecheva, R. Alcántara and J.L. Tirado, *J. Alloys Comp.*, 2009, **475**, 96-101.
36 R. Stoyanova, Sv. Ivanova, E. Zhecheva, Ago Samoson, Sv. Simova, P. Tzvetkova and A.-L Barra, *Phys. Chem. Chem. Phys.*, 2014, **16**, 2499.
37 A. Deb, U. Bergmann, S. Cramer and E. Cairns, *J. Appl. Phys.*, 2006, **99**, 063701.
38 E. Zhecheva, R. Stoyanova, R. Alcántara, P. Lavela and J.L. Tirado, *J. Power Sources*, 2007, **174**, 519.
39 J. Bréger, Y.S. Meng, Y. Hinuma, S. Kumar, K. Kang, Y. Shao-Horn, G. Ceder and C. P. Grey, *Chem. Mater.*, 2006, **18**, 4768.
40 R. Berthelot, M. Pollet, J.P. Doumerc and C. Delmas, *Inorg. Chem.*, 2011, **50**, 6649.
41 Z. Ren, J. Shen, S. Jiang, X. Chen, C. Feng, Z.A. Xu and G.H. Cao, *J. Phys:Condens Matter*, 2006, **18**, L379.
42 J. Bos, J. Hertz, E. Morosan and. R. Cava, *J. Solid State Chem.*, 2007, **180,** 3211.
43 E. Lee, J. Lu, Y. Ren, X. Luo, X. Zhang, J. Wen, D. Miller, A. DeWahl, S. Hackney, B. Key, D. Kim, M.D. Slater and C.S. Johnson, *Adv. Energy Mater.* DOI: 10.1002/aenm.201400458.
44 S. Kim, X. Ma, S.P. Ong and G. Ceder, *Phys. Chem. Chem. Phys.*, 2012, **14**, 15571.
45 X. Xia X and J.R. Dahn, *J Electrochem Soc*, 2012, **159**, A1048-A1051.
46 P.-Y. Brisson, H. Darmstadt, M. Fafard, A. Adnot, G. Servant and G. Soucy, *Carbon*, 2006, **44**, 1438.
47 B. Erdem, R.A. Hunsicker, G.W. Simmons, E.D. Sudol, V.L. Dimonie and M.S. El-Aasser, *Langmuir*, 2001, **17**, 2664.
48 V.I. Nefedov, Y.V. Salyn, G. Leonhardt and R. Scheibe, *J. Electron Spectrosc. Relat. Phenom.*, 1977, **10**, 121.
49 C. Allen, S.J. Harris, J.A. Jutson, J.M. Dyke, *Appl. Surf. Sci.*, 1989, **37**, 111.
50 J.C. Carver, G.K. Schweitzer and T.A. Carlson, *J. Chem. Phys.*, 1972, **57**, 973.
51 A.N. Mansour, *Surf. Sci. Spectra*, 1994, **3**, 279.
52 A.W. Moses, H.G. Garcia Flores, J.-G. Kim and M.A. Langell, *Appl. Surf. Sci.*, 2007, **253**, 4782.
53 R. Schlaf, B.A. Parkinson, P.A. Lee, K.W. Nebesny, G. Jabbour, B. Kippelen, N. Peyghambarian, N.R. Armstrong, *J. Appl. Phys.*, 1998, **84**, 6729.
54 A.M Andersson, M. Herstedt, A. Bishop, K. Edström, *Electrochim. Acta*, 2002, **47**, 1885.
55 T. Eriksson, A.M. Andersson, C. Gejke, T. Gustafsson and J.O. Thomas, *Langmuir* 2002, **18**, 3609-3619.
56 K. Edström, T. Gustafsson and J.O. Thomas, *Electrochim. Acta*, 2004, **50**, 397.
57 R. Dedryvère, S. Leroy, H. Martinez, F. Blanchard, D. Lemordant, D. Gonbeau, *J. Phys. Chem. B*, 2006, **110**, 12986.
58 K. Xu, *Chem. Rev.*, 2004, **104**, 4303.